Unraveling the Global Proteome and Phosphoproteome of Prostate Cancer Patient-Derived Xenografts

Zoi E. Sychev[1], Abderrahman Day[2,3], Hannah E. Bergom[2], Gabrianne Larson[1], Atef Ali[2], Megan Ludwig[1], Ella Boytim[2], Ilsa Coleman[4], Eva Corey[5], Stephen R. Plymate[5,6,7], Peter S. Nelson[4], Justin H. Hwang[2,8,9], and Justin M. Drake[1,9,10]

ABSTRACT

Resistance to androgen-deprivation therapies leads to metastatic castration-resistant prostate cancer (mCRPC) of adenocarcinoma (AdCa) origin that can transform into emergent aggressive variant prostate cancer (AVPC), which has neuroendocrine (NE)-like features. In this work, we used LuCaP patient-derived xenograft (PDX) tumors, clinically relevant models that reflect and retain key features of the tumor from advanced prostate cancer patients. Here we performed proteome and phosphoproteome characterization of 48 LuCaP PDX tumors and identified over 94,000 peptides and 9,700 phosphopeptides corresponding to 7,738 proteins. We compared 15 NE versus 33 AdCa samples, which included six different PDX tumors for each group in biological replicates, and identified 309 unique proteins and 476 unique phosphopeptides that were significantly altered and corresponded to proteins that are known to distinguish these two phenotypes. Assessment of concordance from PDX tumor-matched protein and mRNA revealed increased dissonance in transcriptionally regulated proteins in NE and metabolite interconversion enzymes in AdCa.

Implications: Overall, our study highlights the importance of protein-based identification when compared with RNA and provides a rich resource of new and feasible targets for clinical assay development and in understanding the underlying biology of these tumors.

Introduction

Prostate cancer is the most diagnosed cancer in men in the United States. Early detection via regular screening of serum prostate-specific antigen (PSA) levels has facilitated prostate cancer diagnosis in organ-confined tumors before cancer spreads (1). If a patient presents with aggressive prostate cancer, a classic upfront therapy involves radiation or surgery with androgen-deprivation therapy (ADT; refs. 2, 3). Although ADT response is effective initially, tumors progress to a more aggressive disease known as metastatic castration-resistance prostate cancer (mCRPC; refs. 3, 4). Treatment of mCRPC with adenocarcinoma (AdCa) features consists of hormonal therapies such as enzalutamide, abiraterone acetate, darolutamide, and apalutamide; however, these therapies can often induce novel phenotypes such as aggressive variant prostate cancer (AVPC). AVPC has genetic aberrations, including *PTEN* and *RB1* loss, *TP53* mutations, and diminished androgen receptor (AR) signaling activity. Several definitions of AVPC have been described including treatment-emergent small cell carcinoma, double-negative prostate cancer, amphicrine, or neuroendocrine prostate cancer (NEPC; refs. 5, 6). The emergence of these drug-resistant phenotypes creates a large unmet medical need to identify new protein or phosphoprotein drug targets for potential biomarker and therapeutic development for this subset of CRPC patients.

Analysis of the genomic aberrations has contributed to the understanding of drug resistance mechanisms in prostate cancer. These include mutations and focal amplifications in the *AR*, *PIK3CA/B* mutations, fusions in *BRAF/RAF1*, mutations in *APC*, mutations and amplifications in *CTNNB1*, focal homozygous deletions in *ZBTB16/PLZF*, biallelic loss, inactivation and somatic point mutations in *BRCA1* and *BRCA2*, and biallelic loss and point mutations in *ATM* (7). Additional alterations among other biologically relevant genes include point mutations of *SPOP, FOXA1*, and *TP53*, copy-number alterations in *MYC, RB1, PTEN*, and *CHD1*, and *E26* transformation-specific (ETS) fusions (8–15). The identification of such alterations has paved the way to define pathologic categorizations of mCRPC between AR^+ (AdCa) and AR^- (NE) disease states. These two types of metastatic phenotypes show distinct pathologic features, which in most cases are consequences of the implementation of different treatment modalities with no curative therapies available. In solid tumors, prostate cancer's nonsynchronous mutational rate is in the lower 25% quartile compared with esophageal and colorectal tumors, which are in the higher 75% quartile (7, 16–22). Furthermore, somatic alterations, such as in the PI3K pathway, are present in 49% (73/150) of the mCRPC-afflicted patients, and still half of this population likely will fail to respond if treated with PI3K inhibitors (7, 9, 23). Overall, this information indicates that the genomic feature of prostate cancer explains some of the tumor progression and therapy responses but dismisses key phenotypic functional expression coming from proteins that may be driving the biology and drug resistance.

Several patient-derived xenograft (PDX) tumor models have been developed in prostate cancer reflecting different clinical subtypes including the typical prostate AdCa and the atypical patterns of

[1]Department of Pharmacology, University of Minnesota, Minneapolis, Minnesota. [2]Division of Hematology, Oncology and Transplantation, University of Minnesota, Minneapolis, Minnesota. [3]Institute for Health Informatics, University of Minnesota, Minneapolis, Minnesota. [4]Fred Hutchinson Cancer Center, Seattle, Washington. [5]Department of Urology, University of Washington, Seattle, Washington. [6]Division of Gerontology and Geriatrics Medicine, University of Washington, Seattle, Washington. [7]Geriatric Research Education and Clinical Center, Seattle Veterans Affairs Medical Center, Seattle Washington. [8]Department of Medicine, University of Minnesota Masonic Cancer Center, Minneapolis, Minnesota. [9]Masonic Cancer Center, University of Minnesota, Minneapolis, Minnesota. [10]Department of Urology, University of Minnesota, Minneapolis, Minnesota.

Corresponding Author: Justin M. Drake, Department of Pharmacology, University of Minnesota Medical School, 6-120 Jackson Hall, Minneapolis, MN 55455. E-mail: jdrake@umn.edu

Mol Cancer Res 2024;22:452–64

doi: 10.1158/1541-7786.MCR-23-0976

progression known as AVPC that includes tumors with NE features. These models have been shown to closely reflect the characteristics of the heterogeneity of the patient tumor population, maintaining histopathologic architecture, and the genomic footprint of the tumors from which they were derived (24–28). The LuCaP series has been extensively characterized, including analyses of genomic alterations, transcriptomic profiles, and single tandem repeats (29). However, little is known about the proteomic profiles of these tumors and, specifically, post-translational modifications of these proteins such as phosphorylation.

Recent technological advancements in mass spectrometry (MS)-based proteomics have allowed an increase in protein detection, coverage, and quantification (30, 31). Here, we used Field Asymmetric Ion Mobility Spectrometry (FAIMS; ref. 31) technology and performed a global proteome and phosphoproteome analysis of the LuCaP PDX series to elucidate proteome-wide signatures and unique activated pathways between AdCa and AVPC (with an emphasis on NEPC). We have developed the largest proteome and phosphoproteome database of prostate cancer PDX models, which provides an extensive list of protein targets for drug development, predicted kinase activities, proteins found in blood (plasma), proteins that are secreted, surface proteins, or proteins within biological pathways. Most importantly, we integrated mRNA sequencing data from the same PDX models with our proteomic data and evaluated the concordance between protein and mRNA. The results revealed dissonance between protein and mRNA expression of some important biological targets that would have been dismissed if only mRNA was analyzed from these tumors. Overall, this large proteomic and phosphoproteomic resource will further our understanding of the underlying cell signaling mechanisms, identification and functional validation of novel drug targets, and future biomarker development in prostate cancer.

Materials and Methods

LuCaP PDX tumors

A total of 48 PDX tumors from the LuCaP series (29) representing 18 LuCaP PDX models—6 AdCa noncastrated (NCR) mice, 6 AdCa castrated (CR) mice, and 6 neuroendocrine-like (2–3 independent tumors samples per model)—were used for this analysis. These PDXs were obtained in a frozen pellet that originated from subcutaneously implanted patient-derived advanced prostate cancer from primary tumors and metastatic sites as described previously (29). The age and passage of these tumors are Supplementary Table S1 and the characterization of these PDX tumors shall be found in Nguyen and colleagues (29).

Cell preparation and protein extraction from PDX tumors for proteome and phosphoproteome enrichment

Approximately 150 mg of each tumor was processed as previously described (32). The lysis buffer contained 7 mol/L urea, 2 mol/L thiourea, 0.4 mol/L Tris pH 8.0, 20% acetonitrile (ACN), 10 mmol/L TCEP, 25 mmol/L chloroacetamide, Thermo Scientific's Halt protease inhibitor cocktail 1× concentration (originally 100×), and phosphatase inhibitors (HALT from Thermo). After adding 500 µL of the lysis buffer to the tumor pieces, samples were placed on ice, then vortexed and centrifuged at 12,000 × *g* for 10 minutes. The samples were then sonicated for 5 seconds using a probe sonicator set at 30% amplitude and kept on ice during the entire sonication process. After sonication, the samples were incubated for 0.5 hours at 37°C, then at room temperature for 15 minutes to reduce and alkylate cysteines and centrifuged at 12,000 × *g* for 10 minutes at 18°C. Protein concentration was measured using Bradford Assay (Bio-Rad).

We then used 2.5 mg of protein, added 10 µg of 20 µg/mL lysyl endopeptidase (WAKO, 125-05061) and incubated the samples at room temperature for 5 to 6 hours at pH 7.4. Then adjusted pH to 7.5 to 8.0 using 1 mol/L Tris, pH 11. Then, we added Worthington TPCK-treated trypsin (1 mg/mL) dissolved in 1 mmol/L HCl supplemented with 20 mmol/L of $CaCl_2$ to prevent autolysis. The trypsin mixture was incubated at 4°C for about 1 hour prior to adding to the protein lysate. Samples were diluted 5-fold by adding 10 mmol/L Tris, pH 8.0 to dilute urea <2 mol/L followed by Lys-C and trypsin addition at 1:50 enzyme/protein ratio overnight at 37°C.

After incubation, samples were acidified with TFA to pH 3 or less. Two sequential reverse-phase extraction methods were used first. Hydrophilic–lipophilic balance (HLB) was used first and then the flow through from HLB and wash fractions was vacuum dried, resuspended, and cleaned up again using a C18 solid phase extraction method. The peptides were combined from HLB and C18 cleanups, and peptide yield was measured using the BCA peptide assay (Thermo Fisher Scientific, cat no. 23275). Sample digestion efficiency prior to MS analysis was inspected by evaluating samples before and after enzymatic digestion using SDS-PAGE gels and again after MS analysis.

Mass spectrometry

1 µg of purified peptides was submitted for MS analysis (proteome) and 2 mg of peptides was kept and used for enrichment of phosphopeptides using the Sequential Metal Oxide Affinity Chromatography (SMOAC) Kit (Thermo Fisher; cat no. A32993, A32992). The quantitative analysis of phosphoserine, phosphotyrosine, and phosphothreonine peptides by quantitative MS was performed as previously described (33, 34) with minor modifications in-tandem using the SMOAC assay. The desalted peptide mixture was fractionated online using EASY-spray columns (25 cm^3 × 75 mm ID, PepMap RSLC C18 2 mm). The gradient was delivered by an easy-nano Liquid Chromatography 1000 ultra-high-pressure liquid chromatography system (Thermo Scientific). Tandem mass spectrometry (MS/MS) spectra were collected on the FAIMS TRIBRID mass spectrometer (Thermo Scientific). Samples were run in biological replicates, and raw MS files were analyzed using MaxQuant version 1.4.1.2 (35). MS/MS fragmentation spectra were searched using ANDROMEDA against the UniProt human reference proteome database with canonical and isoform sequences (downloaded August 1st, 2021, from http://uniprot.org). N-terminal acetylation, oxidized methionine, and phosphorylated serine, threonine, or tyrosine were set as variable modifications, and carbamidomethyl cysteine (*C) was set as a fixed modification. The false discovery rate was set to 1% using a composite target-reversed decoy database search strategy. Group-specific parameters included max missed cleavages of two and label-free quantitation (LFQ) with an LFQ minimum ratio count of one. Global parameters included match between runs with a match time and alignment time window of 5 and 20 minutes, respectively, and match unidentified features selected.

MS preprocessing of proteomic and phosphoproteomic data

Maxquant imputed peptide-level raw intensity files were obtained for each sample after the MS runs. At least two peptides had to map to a protein in order to be included in our data analysis for the proteome. We first summed the intensity of duplicated peptides based on the peptide sequences. In considering peptides with missed cleavages, we identified and then summed groups of peptides of variable length but had identical base sequences. We then mapped the peptide sequences to the most likely protein candidate based on algorithms by

MaxQuant (35). We then averaged the intensity of the peptides that belonged to the same protein. To note, this averaging was performed only for the proteomic data and not the phosphoproteomic data. At this stage, we aggregated all samples and then conducted variance stabilization normalization (VSN) for each data set (36, 37). We omitted one 208.1 NEPC sample due to the unexpected expression of AR, which is normally detected only in AdCa. To nominate statistically significant proteins or phospho-peptides, we utilized reproducibility-optimized test statistic (ROTS; ref. 38). FDR-adjusted *P* values were computed which we deemed less than 0.05 as statistically significant. This was used as the threshold for differentially represented features in AdCa or NEPC (Supplementary Tables S4 and S9). We performed this for both proteomic and phosphoproteomic outputs. Hierarchical clustering was performed using the Cluster 3.0 program with the Pearson correlation and pairwise complete linkage analysis (39). Java TreeView was used to visualize clustering results (40). Quantitative data for each peptide and phosphopeptide can be found in Supplementary Tables S2 and S7, respectively, and upstream mapping for each phosphopeptide along with kinase substrate enrichment analysis (KSEA) can be found in Supplementary Tables S10 and S11.

Proteomic and transcriptomic correlation

mRNA data were obtained from the same PDX samples (41) in which we averaged, by sample ID, the $\log_2$ FPKM data for the mRNA sequencing or the VSN normalized protein abundance data. We only included genes that were detected in both data sets and then conducted Spearman correlations between the mRNA expression and protein abundance levels for each gene across all samples. Concordance analysis was done by comparing the hyperabundant proteins from the NE and AdCa groups with the mRNA levels in the transcriptomic data. Concordance indicates that the protein and mRNA fold change is greater than 1.5. Nonconcordance was defined as proteins that are greater than 1.5-fold change, with mRNA between −1.5- and 1.5-fold change. Discordance is defined as proteins that are 1.5-fold change hyper abundant, with mRNA lower than −1.5-fold change. All were statistically significant with an adjusted *P* value of <0.05.

Protein annotations and databases

We analyzed protein functional annotations using Human Proteome Atlas (HPA version 22.0 http://www.proteinatlas.org/) that has categorized blood proteins, secretome (42) and surfaceome (43). Ontologies were identified using gene set enrichment analysis (GSEA version 4.2.1). Potential drug targets were further mapped to gene symbol, to PhosphoSitePlus (44), Therapeutic Target Database (TTD; ref. 45) Genomics of Drug Sensitivity in Cancer (GDSC; ref. 46), and HPA to acquire additional information on whether the targets had drug response data, or they were receptors, kinases, or known cancer/FDA-approved/potential drug targets.

IHC on the LuCaP PDX tissues

The LuCaP UW TMA 103 was constructed from subcutaneous PDX tumors. It contains 39 LuCaP PDX models; 3 tumors per PDX model, and 3 punches per PDX model (together 9 cores per model). The antibodies used for IHC were as follows: HOXB 13 (Cell Signaling Technologies, cat no. #90944, 1:50, antigen retrieval pH6), SYP (Santa Cruz sc-17750, 1:100 antigen retrieval pH6), AR (BioGenex MU256-0717 1:100 Antigen retrieval pH9), ASCL1 (ABCAM ab-211327, 1:100, antigen retrieval pH6). The scoring of each TMA was performed as previously published (29).

Statistical analysis

All statistical data were presented after either *t* tests or ROTS as described in the figure legends. The tumors collected from the PDX models and different mice yielded samples that represented AdCa-CR ($n = 18$), AdCa-NCR ($n = 15$), and NE ($n = 15$). We applied the statistical tests with the assumption that each sample would have independent proteomic and phosphoproteomic profiles.

Data availability

The data can be obtained via the following databases:

LuCaP PDX mRNA sequencing data are available at the Gene-Expression Omnibus under accession GSE199596.

LuCaP PDX phosphoproteome data are available at ProteomeXchange PDX042859.

LuCaP PDX proteome data are available at ProteomeXchange PXD042867.

Results

Proteomic and phosphoproteomic platform analysis

We assessed the global proteome and phosphoproteome of 48 PDX tumor samples, which include 6 different AdCa tumors grown in intact mice (AdCa-NCR, $n = 15$), 6 AdCa grown in castrated mice (AdCa-CR, $n = 18$) and 6 neuroendocrine (NE, $n = 15$) tumors (**Fig. 1A**, sample collection). These samples were all processed in parallel on the same day and bottom-up proteomics was performed (**Fig. 1A**, sample processing). To evaluate the phosphoproteome, we performed phosphotyrosine (pY), phosphoserine (pS), and phosphothreonine (pT) enrichment using a SMOAC assay (**Fig. 1A**, sample processing-II). In parallel, from the pool of peptides prior to phospho-STY enrichment, we used this fraction and evaluated the overall peptide mix, which we defined as the proteome (**Fig. 1A**, sample processing-I). The enriched phosphopeptides and total peptides were analyzed using a state-of-the-art instrument containing a high-FAIMS, which is an atmospheric pressure ion mobility technique that separates gas-phase ions by their behavior in strong and weak electric fields. This approach allows better separation and detection of stable peptides (> +2 charge state ions) for confident quantification (31) compared with no FAIMS application where the instrument collects +1 charge state ions, which are very unstable and not quantifiable, among other advantageous features. We used an in-house proteome and phosphoproteome analysis pipeline (32) that includes MaxQuant (35) for peptide/phosphopeptide searches and data processing (Supplementary Fig. S1). Using a 1% FDR, we identified a total of 94,517 peptides that mapped to 7,738 nonredundant proteins at the proteome level and a total of 9,722 phosphopeptides that mapped to 3,759 nonredundant phosphoproteins (**Fig. 1B** and **C**; Supplementary Tables S2 and S7) with a phosphosite probability > 0.75. In combination, we identified 8,612 unique master proteins from these samples, where 32.6% of these proteins overlapped between the proteome and phosphoproteome data sets whereas 9.9% were unique to the phosphoproteome and 57.5% were unique to the proteome (**Fig. 1D**).

To infer protein abundance, we used intensity-based absolute quantification (iBAQ; ref. 47). To identify the significantly altered proteins, we performed a VSN (36) making the sample variances nondependent from their mean intensities using *P* value adjusted < 0.05 and a $\log_2$ fold change. Using this approach, we identified 147 proteins that were hyper-abundant in the NE group and 162 proteins in the AdCa group (**Fig. 1E**; Supplementary Table S4). Using similar statistical analyses, we identified 259 unique hyperphosphorylated peptides in the NE samples and 217 unique hyperphosphorylated

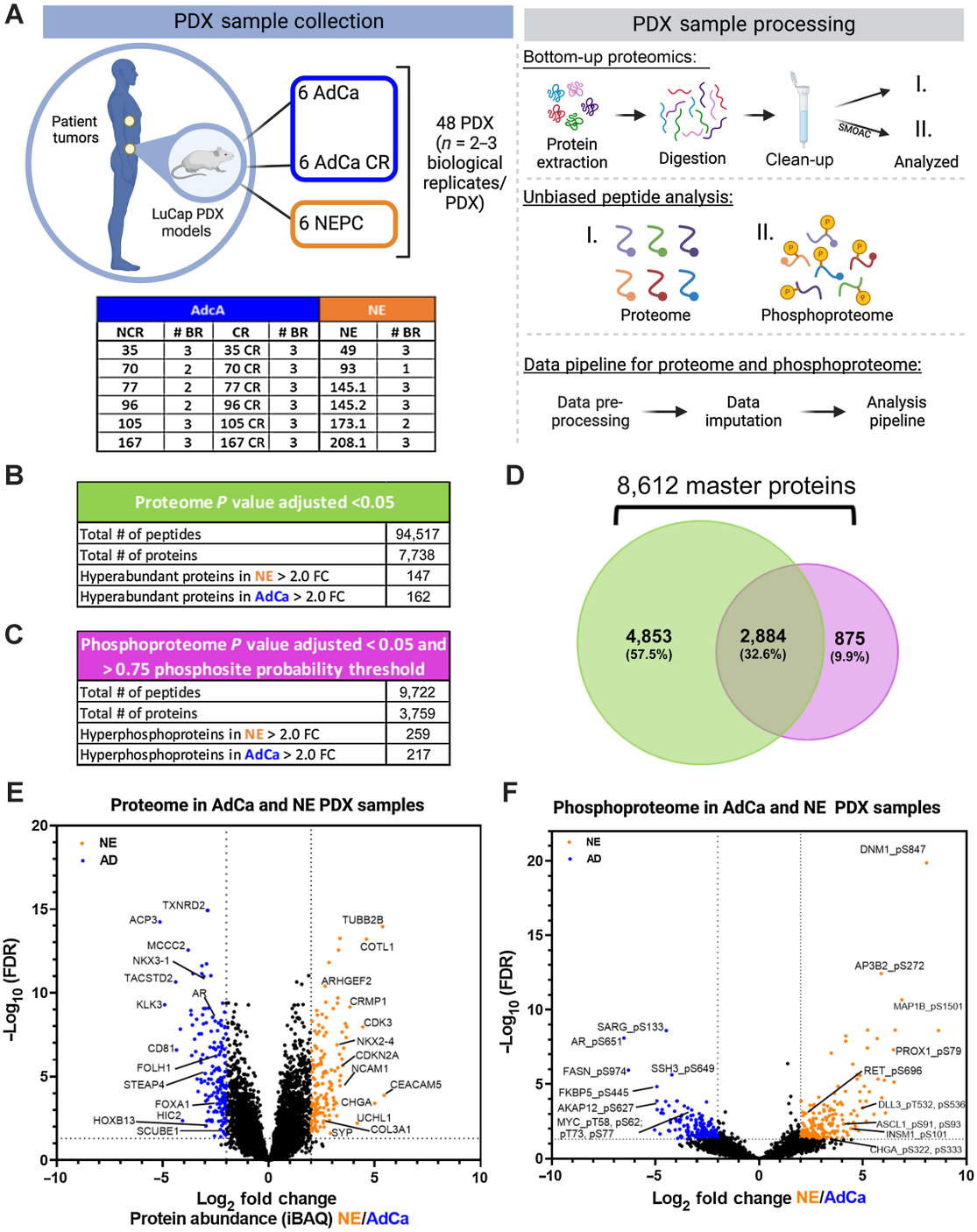

AdcA				NE	
NCR	# BR	CR	# BR	NE	# BR
35	3	35 CR	3	49	3
70	2	70 CR	3	93	1
77	2	77 CR	3	145.1	3
96	2	96 CR	3	145.2	3
105	3	105 CR	3	173.1	2
167	3	167 CR	3	208.1	3

Proteome *P* value adjusted <0.05	
Total # of peptides	94,517
Total # of proteins	7,738
Hyperabundant proteins in NE > 2.0 FC	147
Hyperabundant proteins in AdCa > 2.0 FC	162

Phosphoproteome *P* value adjusted < 0.05 and > 0.75 phosphosite probability threshold	
Total # of peptides	9,722
Total # of proteins	3,759
Hyperphosphoproteins in NE > 2.0 FC	259
Hyperphosphoproteins in AdCa > 2.0 FC	217

Figure 1.

Proteomic and phosphoproteomic platform and characterization. **A,** The LuCaP series of 48 PDX tumors is depicted in the table, where 33 AdCa either castrated and noncastrated tumors are shown in dark blue and 15 NEPC tumors are shown in orange, $n = 2$–3 biological replicates (BR). The PDXs were processed by extracting proteins and an enzymatic digestion was performed using Trypsin and LysC. Peptides were purified by reversed-phase chromatography. The final peptide pool was run as the proteome (I) and in parallel a SMOAC assay was performed to enrich for phosphorylated serine, threonine and tyrosine which was run as the phosphoproteome (II). Finally, raw data were searched, processed, and analyzed. **B,** Overall proteome results using 1% FDR for protein identification and *P* value adjusted < 0.05 $\log_2$ fold change (FC) significance. **C,** Overall proteome results using 1% FDR for phosphoprotein identification and *P* value adjusted <0.05 $\log_2$ fold change (FC) significance and >0.75 phosphosite probability threshold. **D,** Venn diagram of the proteome and phosphoproteome shows the total number of 8,612 master proteins identified when both data sets are overlaid. **E,** Volcano plot of the proteome depicting the intensity-based average quantification (iBAQ) enriched in NE and AdCa. **F,** Volcano plot of the phosphoprotein enriched in NE vs. AdCa. Gray lines in the x-axis and y-axis are the cutoff threshold for NE 2-fold change and for AdCa 2-fold change and *P* value adjusted to ($-\log_{10}$ FDR), respectively in **E–F**.

peptides in the AdCa group (**Fig. 1F**; Supplementary Table S9). We performed several comparisons between AdCa grown in castrated mice (CR) versus AdCa grown in intact, or noncastrated, mice (NCR), AdCa-CR versus NE, and AdCa-NCR plus AdCa-CR (pooled AdCa) versus NE. We made all possible comparisons among the different cohorts such as NCR and CR, CR and NE, and AdCa and NE (Supplementary Tables S18–S26). However, we observed most of the differences between pooled AdCa (NCR + CR) versus NE; therefore, we proceeded with the rest of the analyses comparing NE versus pooled AdCa all.

The LuCaP PDX tumor proteome is consistent with established NE and AdCa gene signatures

To evaluate differences in the overall proteome landscape between NE and the pooled AdCa PDX samples, we performed an unsupervised clustering of all the proteins measured. We observed that there is distinct intertumor variability across all PDX samples (**Fig. 2A**). More specifically, there is more variability across noncastrated (NCR) and castrated (CR) AdCa PDX patient-matched pairs than all of the NE samples, which indicates that the relative protein abundance in NE PDX samples are more similar than we might have expected. We then evaluated if this variability is consistent with the top 50 most highly upregulated proteins across all samples and observed that the intertumor variability mostly disappears in the AdCa PDX samples but clearly clustered uniquely and distinctly from the NE tumors (**Fig. 2B**).

UMAP analysis showed that the PDX tumors clustered within their subgroups (AdCa or NE) despite inter-PDX tumor variability (**Fig. 2C**). Most importantly, individually analyzed proteins that differentiate clinical NEPC (ASCL1, RET, CEACAM5, CHGA, DLL3, SYP, and KIT) from CRPC AdCa (AR, FOXA1, HOXB13, NKX3-1, STEAP1, STEAP4, and TACSTD2) also were hyper-abundant in their corresponding tumor phenotypes (**Fig. 2D–F**; Supplementary Table S3). Four of these proteins (AR, HOXB13, SYP, and ASCL1) were validated on LuCaP tissue microarrays and were indeed expressed primarily in the corresponding tumor phenotype, as expected (Supplementary Fig. S2). Pathway analysis showed that there are 34 pathways enriched in NE and 267 in AdCa. Canonical pathways enriched in the AdCa PDX tumors consisted of sulfide oxidation to sulfate, β-oxidation of very long-chain fatty acids (VLC-FA; **Fig. 2G**; Supplementary Table S5). In the NE PDX tumor samples, we identified an enrichment of proteins involved in the processing and activation of SUMO, ALK2 pathway, polymerase switching, and attachment of GPI anchor to u-PAR (urokinase-type plasminogen activator; **Fig. 2G**). We also observed distinct hallmark gene signatures with oxidative phosphorylation and androgen response, among others enriched in the AdCa PDX tumors whereas E2F targets, G2M checkpoint, and EMT were enriched in the NE PDX tumors (**Fig. 2H**; Supplementary Table S6). These results provide evidence that the PDX tumor protein profiles maintain the proteome architecture and footprint similar to the clinical phenotypes previously observed.

The LuCaP PDX tumor phosphoproteome reveals increased interpatient similarity with established NE and AdCa gene signatures

To evaluate the overall phosphoproteome in the LuCaP PDX samples, we performed a sequential metal oxide phospho-enrichment targeting phosphoserine (pS), phosphothreonine (pT), and phosphotyrosine (pY) residues (**Fig. 1A**, II). Unsupervised hierarchical clustering showed that the AdCa PDX tumors LuCaP 96CR (replicate 10C), 105, 105CR, 167, and 167CR clustered more closely with NE PDX tumors LuCaP 49 (replicate 3A), 145.2, 173.1, and 208.1 whereas the other NE PDX tumors, LuCaP 49 and 145.1, clustered more closely to AdCa PDX tumors LuCaP 35, 35CR, 70, 70CR, 96, 96CR, 77, and 77CR (**Fig. 3A**). This indicates that the phosphoproteome has more interpatient cross-over of similar phosphoproteins between NE and AdCa PDX tumors than the proteome, and the clustering patterns seem to also reflect less interpatient heterogeneity when compared with the proteome. These data provide new insights into the phosphorylation profile of these two mCRPC subgroups where protein phosphorylation reveals more signaling overlap, allowing for the testing of novel drug targets that may treat both AdCa and NE tumors. When clustering the top 50 proteins that mapped to hyper-phosphorylated peptides from each of the AdCa and NE PDX tumors there was distinct segregation between those subgroups; however, there appeared to be a third group (mainly LuCaP 105, 105CR, 167, and 167CR) that clustered with the AdCa tumors but certain phosphoproteins fell somewhere between the AdCa and NE phenotypes (**Fig. 3B**). Although speculative, these tumors may be transitioning from an AdCa to a NE state. Similar to the proteome, we assessed the well-accepted clinical NE and AdCa proteins and mapped them to the phosphoproteome data. Interestingly, these phosphopeptides clustered similarly to the NE and AdCa proteins (**Fig. 2D**) even though most of these phosphoresidues have never been analyzed in this context (**Fig. 3C**; Supplementary Table S8). UMAP analyses also showed that these samples segregated within their corresponding subgroups (**Fig. 3D**), although the AdCa PDX tumor samples were not as tightly clustered as the proteome (**Fig. 2C**), suggesting that a certain group of AdCa PDX tumors may be transitioning toward the NE phenotype. Using the proteins identified from the volcano plot in **Fig. 1F**, we mapped several functional phosphoproteins that have druggable phosphosites (i.e., phosphopeptides that map to phosphoresidues on proteins with known functional activity) that were unique in AdCa (AR_pS651, pS310, pS120; MYC_pT58; RB1_pT373 and SIRT1_pS47) and NE (STMN1_pS38; ADD2_pS697 and pS701; RET_pS696; CDK1_pT161; ARHGEF2_pS956, pS960; MCM2_pS108; EZH2_pT345; USP16_pS552; and E2A_pS379) PDX tumors (**Fig. 3E**; Supplementary Table S9). KSEA was performed to predict other kinase activity within the phosphoproteome data set and found ATM and protein kinase C (PKC) were enriched in the AdCa PDX tumors whereas MAPK activity was enriched in the NE PDX tumors (**Fig. 3F**; Supplementary Tables S10 and S11). Further, pathways involved in the metabolism of RNA, RNA processing, and PID–HIF TF pathway were enriched in AdCa while chromatin modifying enzymes, neurexins and neuroligins, and transcription regulation by RUNX1 were enriched in NE PDX tumors (**Fig. 3G**; Supplementary Table S12). This confirms that NE PDX tumors are more closely related to a neuronal phenotype, whereas AdCa is more metabolically defined. GSEA indicated that androgen response, hypoxia, and MYC targets were enriched in AdCa, whereas G_2–M checkpoint and E2F targets were enriched in the NE PDX tumors (**Fig. 3H**; Supplementary Table S13), as expected and similar to the proteome data. Therefore, despite some interpatient cross-over of AdCa and NE PDX tumors from the global phosphoproteome, there is a significant divergence between AdCa and NE PDX tumors when evaluating the most altered phosphopeptides, including some key druggable targets.

LuCaP PDX tumor proteomic and transcriptomic integration reveals dissonance between mRNA and protein targets

It has been established that mRNA expression has a low to moderate correlation to protein expression with a 40% to 50% concordance (48–50), which might misguide the potential nomination of novel targets if evaluated at the mRNA level only. Previous work on primary prostate cancer tissues observed a weak

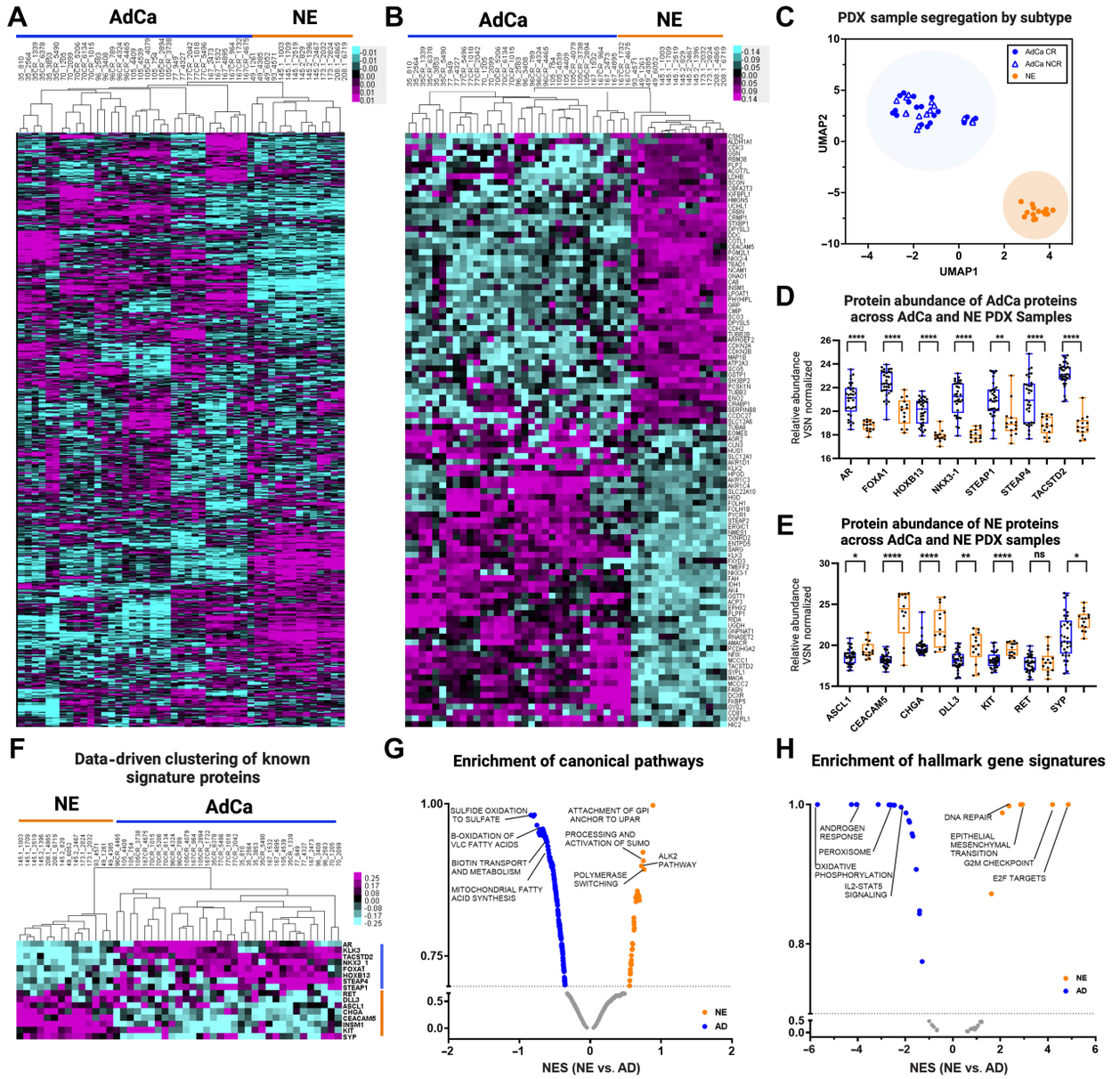

Figure 2.

Proteome landscape of PDXs in prostate cancer. **A,** Unsupervised clustering data drive 7,738 master proteins 1% FDR. **B,** Unsupervised clustering of the top 50 NE and 50 AdCA proteins. **C,** UMAP analysis of all PDXs from the proteome. **D,** The relative abundance of AdCa signature proteins and **E,** NE signature proteins. Blue, AdCa PDX tumors; orange, NE PDX tumors. **F,** Data-driven supervised hierarchical clustering of NE and AdCa signature proteins. **G,** Pathway analysis of NE and AdCa highlighting four of the top pathways on each group. **H,** Hallmarks in cancer analysis of NE and AdCa highlighting four of the top pathways on each group (FDR 0.25).

correlation between mRNA and the corresponding protein expression via MS (median Spearman $\rho = 0.21$; ref. 51). We proceeded to expand upon this and assess the concordance of mRNA and protein on the LuCaP PDX series derived from metastatic CRPC tumors to evaluate potential discrepancy and nominate protein targets confidently for a clinical assay or biomarker development. Importantly, these PDX models provide consistent, reproducible material that will allow us to test and evaluate these discrepancies functionally. The LuCaP PDX mRNA data (41) were analyzed against the LuCaP PDX proteomic data collected in this manuscript. We analyzed and compared the proteins that were statistically significant and hyperabundant (>1.5-fold change) in the NE (336 proteins) and AdCa (360 proteins) PDX tumors with the corresponding matching mRNA transcripts that were statistically significant (matching proteins and mRNA transcripts). We then plotted each protein's relative intensity-based average quantification (iBAQ) $\log_2$ fold change against the correspondent transcript FPKM $\log_2$ fold change, the overall linear regression correlation was low with a statistical significance $r^2 = 0.2359$ as expected from previously published work (ref. 51; Supplementary Fig. S3). Next, we

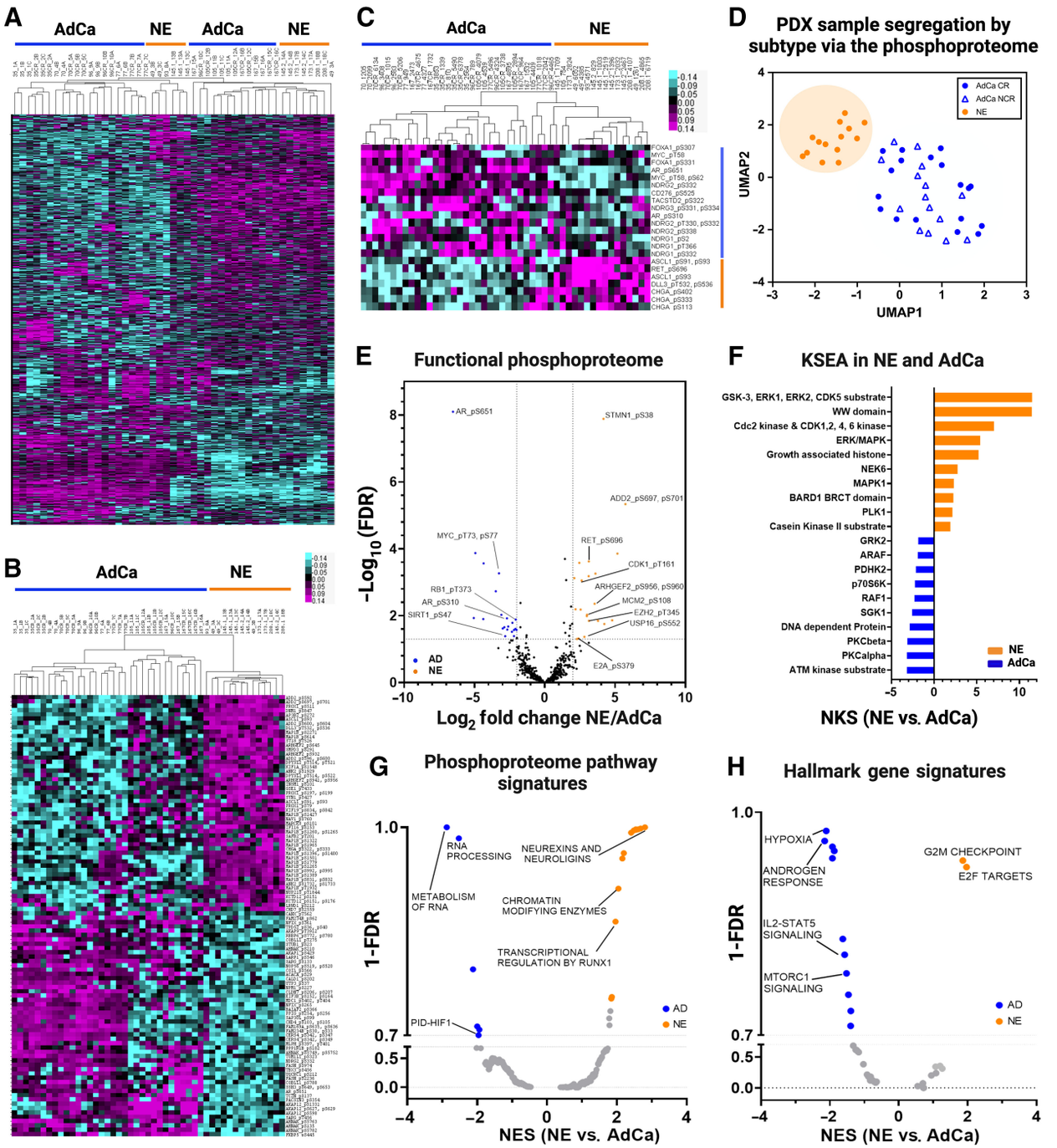

Figure 3.
Phosphoproteome landscape of PDXs in prostate cancer. **A,** Data-driven unsupervised clustering of 9,723 phosphopeptides with 1% FDR. **B,** Unsupervised clustering of top 50 NE and 50 AdCA hyper-phosphorylated peptides. **C,** Unsupervised hierarchical clustering of AdCa and NE signature phosphoproteins. **D,** UMAP analysis of all phosphopeptides. **E,** Volcano plot of functional phosphoproteome of NE and AD hyperphosphorylated peptides. **F,** Kinase/substrate enrichment (KSEA) analysis identified unique and known kinases that were predicted from the phosphoproteome (top 10 hits are shown on each group). **G–H,** GSEA was performed to identify canonical pathways (**F**) and hallmarks in cancer (**G**) enriched in NE (orange) and AdCa (blue). NES, normalized enrichment score; orange, hyperphosphorylated in NE, and blue hyperphosphorylated in AdCa.

performed concordance analysis where we focused only on the hyper-abundant proteins and their matching mRNA expression-level counterparts. Although all the proteins analyzed here were statistically significant and hyper-abundant, we observed that only 54% (NE) and 59% (AdCa) of the matching proteins/mRNA transcripts were concordant (C; mRNA and protein are upregulated and hyper-abundant, respectively) whereas more than 40% in NE and 35% in AdCa proteins were nonconcordant either discordant level I (DC.I; mRNA is not altered/changed significantly and protein is hyper-abundant) or discordant level II (DC.II; mRNA is significantly downregulated whereas the protein is hyper-abundant; **Fig. 4A**). These data strongly indicate that we are missing important drug targets and tumor biology within these two PDX subgroups if we were to focus only on mRNA changes. We then analyzed the directionality of the proteins versus the mRNA counterpart within the subgroups, and the overall dynamic range of mRNA expression was greater in the concordant group than the relative abundance in protein expression (**Fig. 4B**, right side) compared with the nonconcordant groups (DC.I and DC. II; **Fig. 4B**, left side and middle). We then performed two sub-analyses focusing on the AdCa and NE PDX tumors alone to show the overall distribution of the mRNA FPKM versus protein iBAQ fold changes (**Fig. 4C** and **D**). After evaluation of the protein class analysis (**Fig. 4E**), we observed that NE hyper-abundant proteins, which were classified as discordant level I (DC.I) and discordant level II (DC.II), were mainly categorized as transcriptional regulators (such as NKX2-4, SMARCD1, ATF2, ZBTB21, MYEF2, and more), chromatin binding proteins (CENPH), and DNA metabolic proteins (TIPIN). This indicates that the mRNA transcripts of these proteins were not changed or the expression was downregulated, whereas the protein was hyper-abundant (**Fig. 4D**). These targets have relevance in the biology of NEPC and would have been missed if only the mRNA transcripts were analyzed.

To identify if the proteins that are discordant level I (DC.I) and discordant level II (DC.II) share any common characteristics, we performed a gene ontology protein class analysis (**Fig. 4E**). From this, we identified that the proteins involved in chromatin binding, DNA metabolism, chaperon, and protein modifying enzymes were over-represented in the NE discordant level I and discordant level II groups (DC.I + DC.II) compared with AdCa, whereas translational proteins, transporter, scaffold proteins, and metabolite interconversion enzymes were greater in the AdCa DC.I and DC.II groups. These data also show that there was greater dissonance in the NE DC.I and DC.II than in AdCa PDX tumors, indicating that these targets would have been disregarded if only mRNA had been analyzed.

To illustrate an example of extreme discordance patterns between protein and mRNA, such as in DC.II, we show two examples of proteins that are highly abundant in AdCa (HIC2, **Fig. 4F**) and NE (COL3A1, **Fig. 4G**), but the mRNA expression levels are very low. HIC ZBTB Transcriptional Repressor 2 (HIC2), a protein that enables protein C-terminus binding activity, is predicted to be involved in the regulation of transcription by RNA polymerase. In prostate cancer, HIC2 protein expression was shown to be increased in tumors compared with benign hyperplasia and normal tissue with a Gleason score greater than 7 and grade 3 (52). Collagen Type III Alpha 1 Chain (COL3A1) is a protein that is found in most soft connective tissues along with type I collagen (53, 54). It is involved in the regulation of cortical development, and it is the major ligand of ADGRG1 in the developing brain. Moreover, COL3A1 binding to ADGRG1 inhibits neuronal migration and activates the RhoA pathway by coupling ADGRG1 to GNA13 and possibly GNA12 (55). In prostate cancer, COL3A1 is suppressed by miR-29b in DU145. After treatment with the miR-29b inhibitor, COL3A1 expression is increased as well as the cells' invasiveness (54). Therefore, in the case of these two proteins and their vital role in prostate cancer development or metastases, these targets/biomarkers would have been missed if only mRNA was used to analyze differential changes, impeding opportunities toward the possible development of therapies against these proteins.

Systematic analysis of the functional proteome and phosphoproteome for actionable targets

We further investigated the hyper-abundant proteins and phosphoproteins from the NE and AdCa subgroups to identify key biomarkers and drug targets. We used the following databases for our query: the secretome (found in the extracellular matrix; ref. 42) and blood proteins (found in blood plasma) from the HPA, the surfaceome (43) and drug analysis from the Therapeutic Target Database (45), and Genomics of Drug Sensitivity in Cancer (GDSC; ref. 46). We analyzed the proteins that were hyper-abundant (**Fig. 5A** and **B**; Supplementary Tables S16, S17, and S27) and hyper-phosphorylated (**Fig. 5C** and **D**; Supplementary Tables S14, S15, and S28) in AdCa and NE PDXs and searched them against these databases. We included the concordance stratification level on the proteome and for the phosphoproteome, concordance was possible only by mapping the protein concordance level from the proteome to the phosphorylated peptide counterpart (**Fig. 5C** and **D**). Of the 82 and 70 hyper-abundant proteins in AdCa and NE, respectively, 44% (36 proteins) and 36% (25 proteins) have drug targets in different stages of development, whereas over 50% of the remaining proteins would be categorized as novel targets for drug development (**Fig. 5E** and **F**).

At the phosphoproteome level, 16% (2 proteins) and 36% (5 proteins) of the hyperphosphorylated proteins in AdCa and NE, respectively, have drug therapies developed in different stages, whereas the remaining have not been investigated as potential therapeutic targets. Our data identified several proteins and phosphoproteins that would be viable biomarkers and cell-surface proteins that could be used for future biologics such as CAR-T cell therapy, antibody–drug conjugates, and radio-ligand targeted therapy development. Overall, our data demonstrated that there is a strong mRNA/protein concordance for certain protein targets, but other protein targets may have been overlooked or misinterpreted based on mRNA data alone. These new protein targets could provide new insights into prostate cancer biology, identification and development of biomarkers, and drug targets.

Discussion

The continuous emergence of therapeutic resistance to current treatment modalities in mCRPC necessitates the identification of novel prognostic and predictive biomarkers as well as specific targets for personalized patient stratification and the development of new effective therapies. Different prostate cancer PDX models have been developed and evaluated at the transcriptome (26, 28, 56, 57), proteome (28), genome (26, 29), copy-number variation (26, 29), and at the single-cell level (26) to understand the underlying mechanisms of resistance to therapies. Although these models have elucidated some very interesting biology, protein posttranslational modifications, such as phosphorylation, have not been fully explored. In this work, we expanded beyond the proteome to include the phosphoproteome and reported one of the largest global proteomic and phosphoproteomic databases capable of differentiating NE from AdCa in the LuCaP PDX tumor models. With this approach, we combined both the proteome

A

Stratification level	AdCa		NE	
	# of Proteins	% of Total	# of Proteins	% of Total
Concordant (C)	213	59.00	183	54.30
Discordant I (DC.I)	139	35.50	147	43.62
Discordant II (DC.II)	9	2.50	7	2.08

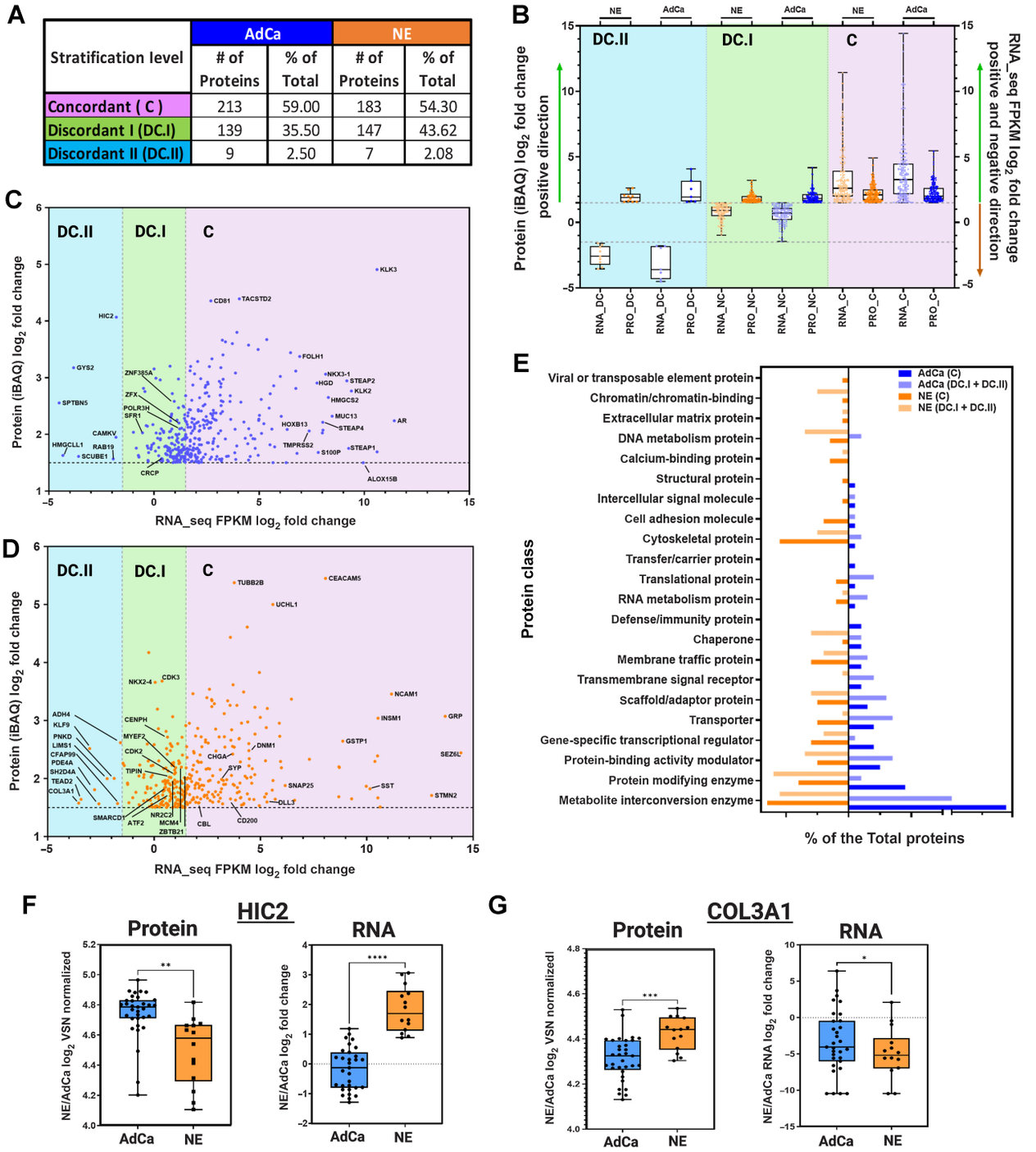

Figure 4.

Proteomic and transcriptomic data integration reveals dissonance of targetable proteins. **A,** The table shows the three main stratification levels of protein and mRNA expression agreements, concordant (C); discordant I (DC.I); discordant II (DC.II) and the total number of hyper-abundant proteins in AdCa ($n = 361$) and in NE ($n = 337$) including percent distribution of total, respectively. **B,** Protein and mRNA $\log_2$ fold change evaluating only the hyper-abundant protein in NE (337 proteins) and AdCa (361 proteins) and simultaneously evaluating the direction of the mRNA expression of those proteins that are stratified as concordant (**C**; mRNA and protein are upregulated and hyper-abundant), discordant I (DC.I; mRNA is not altered significantly and protein is hyper-abundant) and discordant II (DC.II; mRNA is significantly downregulated whereas the protein is hyper-abundant). **C–D,** AdCa and NE hyper-abundant proteins iBAQ (VSN normalized and ROTS *P* value adjusted <0.05 significances) mRNA FPKM (ROTS normalized and *P* value adjusted <0.05) $\log_2$ fold change highlighting proteins of interest. **E,** GO protein class analysis of the NE and AdCa concordant and non-concordant plus discordant proteins. Box plots of protein $\log_2$ fold change VSN normalized and mRNA $\log_2$ fold change of $n = 33$ AdCa and $n = 14$ NE evaluating the overall expression in (**F**) HIC-2 and (**G**) COL3A1. Data are represented as mean ± SEM; **, $P < 0.01$; ***, $P < 0.001$, two-tailed Welch-corrected.

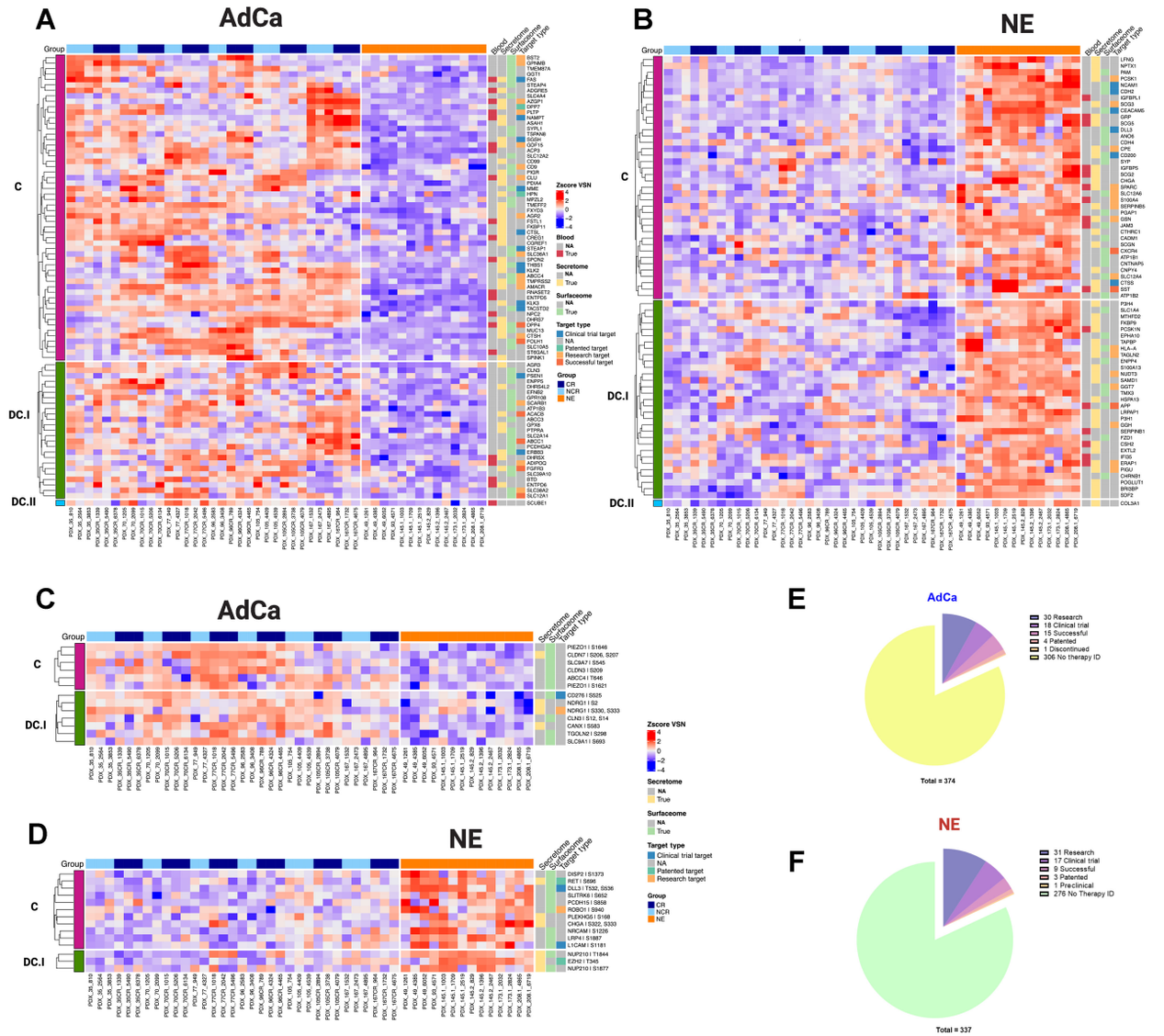

Figure 5.

Functional proteome and phosphoproteome characterization. Heat map data illustrate z-score VSN-normalized protein hyper-abundance expression for AdCa (n = 82; **A**) and NE (n = 70; **B**) Heat map data illustrates z-score VSN normalized proteins hyper-phosphorylated expression for AdCa (n = 13; **C**) and NE (n = 14; **D**). Concordance level was defined by using the master protein counterpart and clustered based on this concordance from the proteome. Pie charts illustrate the therapeutic target distribution identified across the hyper-abundant proteins in AdCa (**E**) with a total of 337 and NE (**F**) with a total of 374 analyzed. Functional proteins color coding that are identified as blood (red), secreted (yellow) surface (light green), and therapy target type such as clinical trial in blue, patented in green, research target in light orange, successful in terracotta, and no available data identified as NA in gray.

and phosphoproteome and we were able to measure over 8,600 proteins and demonstrated inter-PDX tumor variability. Furthermore, a comparison of individual AdCa-matched tumor pairs grown in noncastrated (NCR) versus castrated (CR) mice showed that their proteome and phosphoproteome signals were mainly unchanged and the differences between the pairs were not significant (**Fig. 2A** and **B**; **Fig. 3A** and **B**; Supplementary Tables S18–S26). Interestingly, unsupervised clustering analysis of the phosphoproteome revealed that select neuroendocrine PDXs (LuCaP 49, 93, 145.1) clustered with the majority of the AdCa PDXs, whereas select AdCa PDXs (LuCaP 105, 105CR, 167, and 167 CR) clustered more closely with the majority of the NE PDXs. However, when selecting the top 50 most phosphorylated proteins from both NE and AdCa, the separation between these two groups was more apparent, highlighting that the differences between these groups are within the most hyperphosphorylated proteins. In addition, detected phosphorylated proteins such as AR, MYC, NDRG1, NDRG2 FOXA1, TACSTD2 in AdCa PDXs, and ASCL1, RET, DLL3, CHGA in NE PDXs clustered with their known protein/gene signature counterpart (**Fig. 3D**). The characterization of the unsupervised and supervised clustering of these phosphorylated peptides at a global scale is relatively new in prostate cancer since phosphoprotein signatures have not been established or defined to

date. However, we can clearly observe that the detected phosphorylated proteins fall within their respective disease phenotype.

Although the genome is typically constant, the proteome is quite different from cell to cell, both spatially and temporally. Proteins have over 400 posttranslational modifications, so the diversity generated from a single protein is larger than that of the corresponding gene (58, 59). Many attempts have been made to correlate mRNA with proteins (35, 49, 50). This has uncovered that for a given amount of protein to be translated, it will depend on the gene classification that is transcribed such as a metabolic gene (required for survival) versus a transcription factor (will be turned on/off or degraded as needed for different biological responses), the current cell state, and the posttranslational modification that is driving the signal. Based on this information, we proceeded to integrate the transcriptomic (41) data into the current proteome data in this article. There were two main goals of this work: (i) to investigate concordance/discordance of mRNA and protein expression and (ii) to identify protein-based biomarkers that can lead to the identification or development of therapeutic targets. We initially performed a traditional Spearman correlation that did not identify any significant targets due to small sample size (Supplementary Fig. S3). However, we were able to evaluate the overall dissonance between mRNA and proteins by comparing the directionality of the differential protein expression (focusing on the hyper-abundant) and mRNA (focusing on any directionality: upregulated, downregulated, or not changed) expression of NE versus pooled AdCa PDXs. Interestingly, several of the proteins known to be involved in prostate cancer biology showed discordance between protein and mRNA levels, a finding that may have future clinical disease management implications.

NEPC has been defined as a disease that is highly transcriptionally active regulating proteins involved in DNA replication (for example DNA polymerase, thymidine kinase, dihydrofolate reductase and cdc6), and chromosomal regulation (60), whereas prostate cancer AdCa that expresses AR and without neuroendocrine features is highly metabolically (61) regulated. Furthermore, it has been shown that mRNA from transcription factors have increased average decay rates compared with other mRNA transcripts and are enriched for "fast-decaying" mRNA transcripts with half-lives <2 hours (48). On the other hand, mRNAs related to biosynthetic proteins have decreased decay rates and are deficient in fast-decaying mRNAs (48, 49). This discordance can be explained further by comparing half-lives between proteins and mRNA as well as the timing of data collection. As an example, there are proteins involved in RNA metabolism that would have been missed since the mRNA molecules would have degraded much faster (2–10 hours) than their respective proteins (10–46 hours; ref. 62). Therefore, the identification of discordance observed between mRNA and protein expression levels in these two CRPC disease states (NE vs. AdCa) might be explained mainly by the nature of the proteins expressed in that tumor type and/or the timing of data collection. There are some current algorithms that implement different variables (time and space), including protein isoforms, that could potentially increase the probability of mRNA/protein predictability, but these are still a way off from true implementation (63). Thus, prediction of protein abundance or activity in either AdCa or NE tumors based on mRNA transcript levels alone may be misleading and nominating biomarkers or subsequently designing clinical assays based on the most stable molecule, such as proteins, and evaluating if these proteins are either metabolically or transcriptionally involved will be highly recommended for assay development decision-making.

The limitation of this study, as well as other studies similar to this that use mouse models, is that there is an 80% gene homology between human and mouse protein-coding genes, implying that some of our identified peptides may map to the mouse proteome (64). Importantly, our study showed that the analyzed LuCaP PDX models have a high degree of similarity with known AdCa and neuroendocrine-like phenotypes and recapitulate many of the underlying mechanisms present in human CRPC. Confirmation and follow-up studies, such as western blot analysis, evaluating the expression of the protein of interest identified from mouse models is recommended using human tissue or cell lines. Our work also revealed a very interesting observation: the global phosphoproteome data intersected between AdCa and NE phenotypes indicating a hierarchy of signaling that is somewhat consistent or maintained across these phenotypes. Importantly, these phosphoproteins could help identify new druggable targets that overlap across prostate cancer phenotypes. Unfortunately to date, the use of phosphoprotein analyses and signature generation is currently hindered by the ability to generate robust phosphoprotein data from small tissue amounts in clinical samples.

In conclusion, we generated the largest proteome and phosphoproteome resource database on clinically relevant and widely used CRPC LuCaP PDX models. Our analysis showed that the overall proteome maintained its fidelity with known CRPC AdCa (AR^+) and NE (AR^-) markers. We found proteins that are known to be overexpressed and hyper-phosphorylated such as AR, RET, ASCL1, DLL3, KIT, CECAM, PSMA/FOHL1, and novel proteins specifically with important functional characteristics for biomarker or drug development, such as surface localization, secreted to the extracellular matrix and/or found in blood plasma. Furthermore, our analyses showed that there is discordance between multiple proteins and their mRNA counterpart that is more dominantly found in transcriptionally regulated proteins compared with metabolic proteins. Future follow-up studies where both mRNA and proteins are collected at the same time and measured in parallel, will be highly recommended to rule in/out any temporal changes that might affect the mRNA levels to the protein expression. Moving forward, we encourage multiomic level analysis, including incorporating the proteome, as a vital element for biomarker and drug development and for effective personalized medicine.

Authors' Disclosures

M. Ludwig reports grants from NCI T32 5T32CA009138-48 during the conduct of the study. E. Corey reports grants from NCI during the conduct of the study. P.S. Nelson reports grants from Janssen, personal fees from Pfizer, Bristol Myers Squibb, and Janssen outside the submitted work. J.M. Drake reports grants, personal fees, and other support from Astrin Biosciences outside the submitted work. No disclosures were reported by the other authors.

Authors' Contributions

Z.E. Sychev: Conceptualization, data curation, formal analysis, validation, investigation, visualization, methodology, writing–original draft. **A. Day:** Formal analysis, writing–review and editing. **H.E. Bergom:** Formal analysis, writing–review and editing. **G. Larson:** Methodology, writing–review and editing. **A. Ali:** Formal analysis, writing–review and editing. **M. Ludwig:** Formal analysis, writing–review and editing. **E. Boytim:** Formal analysis, writing–review and editing. **I. Coleman:** Resources, writing–review and editing. **E. Corey:** Resources, writing–review and editing. **S.R. Plymate:** Resources, writing–review and editing. **P.S. Nelson:** Resources, writing–review and editing. **J.H. Hwang:** Formal analysis, supervision, visualization, writing–review and editing. **J.M. Drake:** Conceptualization, data curation, formal analysis, supervision, funding acquisition, validation, investigation, methodology, writing–original draft, writing–review and editing.

Acknowledgments

Z.E. Sychev is supported by the Department of Defense Prostate Cancer Research Program E01 W81XWH-20-1-0070-P00002 and the Molecular, Genetic, and Cellular Targets of Cancer Training Program. The establishment and characterization of the LuCaP PDX models were supported by the Pacific Northwest Prostate Cancer SPORE P50 CA97186, the P01 NIH grant CA163227, and the Institute for Prostate Cancer Research. P.S. Nelson and I. Coleman are supported by the NIH R01CA234715 and

NIH R21CA277368. S.R. Plymate would like to thank the Veterans Affairs Research and Development Service. We would like to thank the Comparative Medicine Animal Caregivers for assistance with the LuCaP PDX maintenance and the patients and their families who generously donated tissues that made this research possible. J.M. Drake is supported by the NIH R01CA269801 and the Department of Defense Prostate Cancer Research Program W81XWH-18-1-0542. The content is solely the responsibility of the authors and does not necessarily represent the official views of the NIH.

Note

Supplementary data for this article are available at Molecular Cancer Research Online (http://mcr.aacrjournals.org/).

Received November 21, 2023; revised January 26, 2024; accepted February 8, 2024; published first February 12, 2024.

References

1. Stephan C, Rittenhouse H, Hu X, Cammann H, Jung K. Prostate-specific antigen (PSA) screening and new biomarkers for prostate cancer (PCa). EJIFCC 2014;25:55–78.
2. Watson PA, Arora VK, Sawyers CL. Emerging mechanisms of resistance to androgen receptor inhibitors in prostate cancer. Nat Rev Cancer 2015;15:701–11.
3. Wadosky KM, Koochekpour S. Androgen receptor splice variants and prostate cancer: From bench to bedside. Oncotarget 2017;8:18550–76.
4. Antonarakis ES, Armstrong AJ, Dehm SM, Luo J. Androgen receptor variant-driven prostate cancer: clinical implications and therapeutic targeting. Prostate Cancer Prostatic Dis 2016;19:231–41.
5. Beltran H, Prandi D, Mosquera JM, Benelli M, Puca L, Cyrta J, et al. Divergent clonal evolution of castration-resistant neuroendocrine prostate cancer. Nat Med 2016;22:298–305.
6. Abida W, Cyrta J, Heller G, Prandi D, Armenia J, Coleman I, et al. Genomic correlates of clinical outcome in advanced prostate cancer. Proc Natl Acad Sci USA 2019;116:11428–36.
7. Robinson D, Van Allen EM, Wu Y-M, Schultz N, Lonigro RJ, Mosquera J-M, et al. Integrative clinical genomics of advanced prostate cancer. Cell 2015;161:1215–28.
8. Baca SC, Prandi D, Lawrence MS, Mosquera JM, Romanel A, Drier Y, et al. Punctuated evolution of prostate cancer genomes. Cell 2013;153:666–77.
9. Taylor BS, Schultz N, Hieronymus H, Gopalan A, Xiao Y, Carver BS, et al. Integrative genomic profiling of human prostate cancer. Cancer Cell 2010;18:11–22.
10. Berger MF, Lawrence MS, Demichelis F, Drier Y, Cibulskis K, Sivachenko AY, et al. The genomic complexity of primary human prostate cancer. Nature 2011;470:214–20.
11. Barbieri CE, Baca SC, Lawrence MS, Demichelis F, Blattner M, Theurillat J-P, et al. Exome sequencing identifies recurrent SPOP, FOXA1 and MED12 mutations in prostate cancer. Nat Genet 2012;44:685–9.
12. Tomlins SA, Laxman B, Dhanasekaran SM, Helgeson BE, Cao X, Morris DS, et al. Distinct classes of chromosomal rearrangements create oncogenic ETS gene fusions in prostate cancer. Nature 2007;448:595–9.
13. Pflueger D, Terry S, Sboner A, Habegger L, Esgueva R, Lin P-C, et al. Discovery of non-ETS gene fusions in human prostate cancer using next-generation RNA sequencing. Genome Res 2011;21:56–67.
14. Wang X-S, Shankar S, Dhanasekaran SM, Ateeq B, Sasaki AT, Jing X, et al. Characterization of KRAS rearrangements in metastatic prostate cancer. Cancer Discov 2011;1:35–43.
15. Cooper CS, Eeles R, Wedge DC, Van Loo P, Gundem G, Alexandrov LB, et al. Analysis of the genetic phylogeny of multifocal prostate cancer identifies multiple independent clonal expansions in neoplastic and morphologically normal prostate tissue. Nat Genet 2015;47:367–72.
16. Lam H-M, McMullin R, Nguyen HM, Coleman I, Gormley M, Gulati R, et al. Characterization of an abiraterone ultraresponsive phenotype in castration-resistant prostate cancer patient-derived xenografts. Clin Cancer Res 2017;23:2301–12.
17. Nguyen B, Mota JM, Nandakumar S, Stopsack KH, Weg E, Rathkopf D, et al. Pan-cancer analysis of CDK12 alterations identifies a subset of prostate cancers with distinct genomic and clinical characteristics. Eur Urol 2020;78:671–9.
18. Nickols NG, Nazarian R, Zhao SG, Tan V, Uzunangelov V, Xia Z, et al. MEK-ERK signaling is a therapeutic target in metastatic castration resistant prostate cancer. Prostate Cancer Prostatic Dis 2019;22:531–8.
19. Pascal LE, Vêncio RZ, Vessella RL, Ware CB, Vêncio EF, Denyer G, et al. Lineage relationship of prostate cancer cell types based on gene expression. BMC Med Genomics 2011;4:46.
20. Vogelstein B, Papadopoulos N, Velculescu VE, Zhou S, Diaz LA, Kinzler KW, et al. Cancer genome landscapes. Science 2013;339:1546–58.
21. Armenia J, Wankowicz SAM, Liu D, Gao J, Kundra R, Reznik E, et al. The long tail of oncogenic drivers in prostate cancer. Nat Genet 2018;50:645–51.
22. Garraway LA, Lander ES. Lessons from the cancer genome. Cell 2013;153:17–37.
23. Schwartz S, Wongvipat J, Trigwell CB, Hancox U, Carver BS, Rodrik-Outmezguine V, et al. Feedback suppression of PI3Kalpha signaling in PTEN-mutated tumors is relieved by selective inhibition of PI3Kbeta. Cancer Cell 2015;27:109–22.
24. Lin D, Wyatt AW, Xue H, Wang Y, Dong X, Haegert A, et al. High fidelity patient-derived xenografts for accelerating prostate cancer discovery and drug development. Cancer Res 2014;74:1272–83.
25. Shi M, Wang Y, Lin D, Wang Y. Patient-derived xenograft models of neuroendocrine prostate cancer. Cancer Lett 2022;525:160–9.
26. Risbridger GP, Clark AK, Porter LH, Toivanen R, Bakshi A, Lister NL, et al. The MURAL collection of prostate cancer patient-derived xenografts enables discovery through preclinical models of uro-oncology. Nat Commun 2021;12:5049.
27. Palanisamy N, Yang J, Shepherd PDA, Li-Ning-Tapia EM, Labanca E, Manyam GC, et al. The MD Anderson prostate cancer patient-derived xenograft series (MDA PCa PDX) captures the molecular landscape of prostate cancer and facilitates marker-driven therapy development. Clin Cancer Res 2020;26:4933–46.
28. Flores-Morales A, Bergmann TB, Lavallee C, Batth TS, Lin D, Lerdrup M, et al. Proteogenomic characterization of patient-derived xenografts highlights the role of REST in neuroendocrine differentiation of castration-resistant prostate cancer. Clin Cancer Res 2019;25:595–608.
29. Nguyen HM, Vessella RL, Morrissey C, Brown LG, Coleman IM, Higano CS, et al. LuCaP prostate cancer patient-derived xenografts reflect the molecular heterogeneity of advanced disease and serve as models for evaluating cancer therapeutics. Prostate 2017;77:654–71.
30. Hebert AS, Prasad S, Belford MW, Bailey DJ, McAlister GC, Abbatiello SE, et al. Comprehensive single-shot proteomics with FAIMS on a hybrid orbitrap mass spectrometer. Anal Chem 2018;90:9529–37.
31. Swearingen KE, Moritz RL. High-field asymmetric waveform ion mobility spectrometry for mass spectrometry-based proteomics. Expert Rev Proteomics 2012;9:505–17.
32. Drake JM, Paull EO, Graham NA, Lee JK, Smith BA, Titz B, et al. Phosphoproteome integration reveals patient-specific networks in prostate cancer. Cell 2016;166:1041–54.
33. Cheng LC, Li Z, Graeber TG, Graham NA, Drake JM. Phosphopeptide enrichment coupled with label-free quantitative mass spectrometry to investigate the phosphoproteome in prostate cancer. J Vis Exp 2018;(138):57996.
34. Nita-Lazar A, Saito-Benz H, White FM. Quantitative phosphoproteomics by mass spectrometry: past, present, and future. Proteomics 2008;8:4433–43.
35. Cox J, Mann M. MaxQuant enables high peptide identification rates, individualized p.p.b.-range mass accuracies and proteome-wide protein quantification. Nat Biotechnol 2008;26:1367–72.
36. Huber W, von Heydebreck A, Sultmann H, Poustka A, Vingron M. Variance stabilization applied to microarray data calibration and to the quantification of differential expression. Bioinformatics 2002;18 Suppl 1:S96–104.
37. Valikangas T, Suomi T, Elo LL. A systematic evaluation of normalization methods in quantitative label-free proteomics. Brief Bioinform 2018;19:1–11.
38. Suomi T, Seyednasrollah F, Jaakkola MK, Faux T, Elo LL. ROTS: an R package for reproducibility-optimized statistical testing. PLoS Comput Biol 2017;13:e1005562.
39. Eisen MB, Spellman PT, Brown PO, Botstein D. Cluster analysis and display of genome-wide expression patterns. Proc Natl Acad Sci USA 1998;95:14863–8.
40. Saldanha AJ. Java treeview–extensible visualization of microarray data. Bioinformatics 2004;20:3246–8.
41. Coleman IM, DeSarkar N, Morrissey C, Xin L, Roudier MP, Sayar E, et al. Therapeutic implications for intrinsic phenotype classification of metastatic castration-resistant prostate cancer. Clin Cancer Res 2022;28:3127–40.

42. Uhlén M, Karlsson MJ, Hober A, Svensson A-S, Scheffel J, Kotol D, et al. The human secretome. Sci Signal 2019;12:eaaz0274.
43. Bausch-Fluck D, Goldmann U, Müller S, van Oostrum M, Müller M, Schubert OT, et al. The in silico human surfaceome. Proc Natl Acad Sci USA 2018;115: E10988–97.
44. Hornbeck PV, Zhang B, Murray B, Kornhauser JM, Latham V, Skrzypek E, et al. PhosphoSitePlus, 2014: mutations, PTMs and recalibrations. Nucleic Acids Res 2015;43:D512–520.
45. Zhou Y, Zhang Y, Lian X, Li F, Wang C, Zhu F, et al. Therapeutic target database update 2022: facilitating drug discovery with enriched comparative data of targeted agents. Nucleic Acids Res 2022;50:D1398–407.
46. Yang W, Soares J, Greninger P, Edelman EJ, Lightfoot H, Forbes S, et al. Genomics of drug sensitivity in cancer (GDSC): a resource for therapeutic biomarker discovery in cancer cells. Nucleic Acids Res 2013;41:D955–961.
47. Schwanhäusser B, Busse D, Li N, Dittmar G, Schuchhardt J, Wolf J, et al. Global quantification of mammalian gene expression control. Nature 2011; 473:337–42.
48. Yang E, van Nimwegen E, Zavolan M, Rajewsky N, Schroeder M, Magnasco M, et al. Decay rates of human mRNAs: correlation with functional characteristics and sequence attributes. Genome Res 2003;13:1863–72.
49. Liu Y, Beyer A, Aebersold R. On the dependency of cellular protein levels on mRNA abundance. Cell 2016;165:535–50.
50. Maier T, Guell M, Serrano L. Correlation of mRNA and protein in complex biological samples. FEBS Lett 2009;583:3966–73.
51. Sinha A, Huang V, Livingstone J, Wang J, Fox NS, Kurganovs N, et al. The proteogenomic landscape of curable prostate cancer. Cancer Cell 2019;35:414–27.
52. Gaballah MSA, Ali HEA, Hassan ZA, Mahgoub S, Ali HI, Rhim JS, et al. Small extracellular vesicle-associated miR-6068 promotes aggressive phenotypes of prostate cancer through miR-6068/HIC2/SIRT1 axis. Am J Cancer Res 2022;12: 4015–27.
53. Jia D, Zhou Z, Kwon O-J, Zhang L, Wei X, Zhang Y, et al. Stromal FOXF2 suppresses prostate cancer progression and metastasis by enhancing antitumor immunity. Nat Commun 2022;13:6828.
54. Ivanovic RF, Viana NI, Morais DR, Silva IA, Leite KR, Pontes-Junior J, et al. miR-29b enhances prostate cancer cell invasion independently of MMP-2 expression. Cancer Cell Int 2018;18:18.
55. Engqvist H, Parris TZ, Kovács A, Nemes S, Werner Rönnerman E, De Lara S, et al. Immunohistochemical validation of COL3A1, GPR158 and PITHD1 as prognostic biomarkers in early-stage ovarian carcinomas. BMC Cancer 2019;19:928.
56. Iglesias-Gato D, Thysell E, Tyanova S, Crnalic S, Santos A, Lima TS, et al. The proteome of prostate cancer bone metastasis reveals heterogeneity with prognostic implications. Clin Cancer Res 2018;24:5433–44.
57. Iglesias-Gato D, Wikström P, Tyanova S, Lavallee C, Thysell E, Carlsson J, et al. The proteome of primary prostate cancer. Eur Urol 2016;69:942–52.
58. Ramazi S, Zahiri J. Posttranslational modifications in proteins: resources, tools and prediction methods. Database (Oxford) 2021;2021:baab012.
59. Conibear AC. Deciphering protein post-translational modifications using chemical biology tools. Nat Rev Chem 2020;4:674–95.
60. Xia H, Wang M, Su X, Lv Z, Yan Q, Guo X, et al. A novel gene signature associated with "E2F Target" pathway for predicting the prognosis of prostate cancer. Front Mol Biosci 2022;9:838654.
61. Ahmad F, Cherukuri MK, Choyke PL. Metabolic reprogramming in prostate cancer. Br J Cancer 2021;125:1185–96.
62. Moss Bendtsen K, Jensen MH, Krishna S, Semsey S. The role of mRNA and protein stability in the function of coupled positive and negative feedback systems in eukaryotic cells. Sci Rep 2015;5:13910.
63. Magnusson R, Rundquist O, Kim MJ, Hellberg S, Na CH, Benson M, et al. RNA-sequencing and mass-spectrometry proteomic time-series analysis of T-cell differentiation identified multiple splice variants models that predicted validated protein biomarkers in inflammatory diseases. Front Mol Biosci 2022;9:916128.
64. Breschi A, Gingeras TR, Guigo R. Comparative transcriptomics in human and mouse. Nat Rev Genet 2017;18:425–40.